Far-infrared emission from graphene on SiC by current injection

Taichi Kataoka[1]*, Fumiya Fukunaga[1], Naruse Murakami [2], Yoshiki Sugiyama[2], Yasuhide Ohno[1-3], and Masao Nagase[1-3]*

[1]*Graduate School of Sciences and Technology for Innovation, Tokushima University, 2-1, Minami-josanjima cho, Tokushima, Tokushima 770-8506, Japan*

[2]*Graduate School of Advanced Technology and Science, Tokushima University, 2-1, Minami-josanjima cho, Tokushima, Tokushima 770-8506, Japan*

[3]*Institute of Post-LED Photonics, Tokushima University, 2-1, Minami-josanjima cho, Tokushima, Tokushima 770-8506, Japan.*

*E-mail: t_kataoka@ee.tokushima-u.ac.jp, nagase@ee.tokushima-u.ac.jp

The far-infrared emission properties of epitaxial graphene on SiC obtained by current injection were investigated using an infrared camera and Fourier-transform infrared spectroscopy. The radiation directivity from the graphene emitter was observed in the directions perpendicular to the surface and edge of the sample. The emission energy density from the graphene edge was larger than that from the graphene surface in all directions. The maximum measured temperature change at 0.4 W for the edge emission was 76.1 K for a tilt angle of 50° and that for the surface emission was 54.1 K for 0°. A blackbody-like emission spectrum with a constant peak wavelength of 10.0 μm, regardless of the applied electrical power, was observed for both the surface and edge. A far-infrared light emitter was successfully realized using single-crystal graphene on SiC.

1. Introduction

Graphene, a two-dimensional material, is expected to be applied in a wide range of fields[1] owing to its unique characteristics[2,3], such as zero bandgap and high carrier mobility. For photonic applications, graphene-based devices were investigated theoretically and experimentally, e.g., photodetectors[4-6], optical modulators[7,8], waveguides[9,10], and light emitters[11-14]. Electrically biased graphene[15,16], which is a photon emitter platform, has attracted considerable attention because of simple conversion of electrical power into optical power based on blackbody radiation by Joule heating. Biased-graphene emitters realized ultrafast responsivity[17.18] and tunability via metamaterial[19,20], plasmonic oscillation[21,22] and photonic cavities[23,24]. However, the emission area and emission efficiency of previous biased graphene emitters reached only the micro scale and orders of $\sim 10^{-4}$ [18,23], respectively. Recently, stacked graphene P-N junction diodes constructed using large-area (100 mm^2) graphene on SiC were developed with a high emission efficiency of 10%[25]. Blackbody-like emission with constant peak wavelength (10.2 μm), regardless of the electrical power, based on a non-thermal mechanism was also reported. Exploring fundamental physics of far infrared emission from the biased graphene is critical for establishment of a new platform for developing high-power, high-efficiency infrared emitters.

In this study, we demonstrate the radiation properties of electrically biased single-crystal graphene films epitaxially grown on a SiC substrate. The current was injected from two electrodes at the corners of a 100 mm^2 graphene sample. Infrared emissions from the surface and edge of graphene sample were observed using an infrared camera and Fourier-transform infrared (FTIR) spectroscopy. The radiation directivity, which is the angle dependency of the emission power, was measured for the surface and edge using an infrared camera. The radiation directivity for the sample surface was similar to that of the gray body emission directivity. In contrast, the radiation intensity from the sample edge was almost constant. The emission spectra from the surface and edge were blackbody-like, with a constant peak wavelength, regardless of the electrical power. A far-infrared light-emitting device was established using single-crystal graphene on SiC with current injection.

2. Experimental methods

A graphene sample on 10×10 mm^2 4H-SiC (0001) was prepared using a thermal

decomposition method in an Ar atmosphere[26]. The sheet resistance of the graphene sample was 1510 Ω/sq. The graphene sample was fixed using four gold-coated metal probes, as shown in Fig. 1(a). Gold foils were placed between the graphene sample and probes to reduce the contact resistance. The electrical biasing of the sample was performed using a two-channel source measurement unit (Keithley 2614 B). The maximum two-terminal voltage is 200 V. The applied voltage for the graphene sample was measured using the other two probes in the van der Pauw configuration[27]. The sample was set up during the tilting stage, as shown in Fig. 1(b). The thermal images of the sample were observed using an infrared camera (FLIR T540) at various tilt angles for the measurement of radiation directivity. Since the energy density of far-infrared (7.5-14 μm) was measured by the infrared camera with micro-electrical-mechanical system (MEMS) bolometer, the measured temperature in this paper represented the intensity of far-infrared emission form the samples. The tilt angle θ was defined as the angle between the normal to the graphene surface and the infrared camera. When θ was 0°, only emissions from the sample surface were observed. When θ was 90°, only emissions from the sample edge were observed. The thermal images were taken in air with an emissivity of 0.95. The infrared radiation spectrum from the biased sample was measured using an FTIR spectrometer (Jasco FT/IR-6600) in air.

3. Results and discussion

3.1 Infrared image of biased graphene

Figure 2(a) shows an optical image of the device at a tilt angle of 60°. In the figure, the regions surrounded by the blue and red squares indicate the surface and edge regions, respectively. Figure 2(b) shows the infrared image of the biased sample at 0.4 W. Since the temperature was measured by the MEMS bolometer with the emissivity of 0.95, the temperature values in the thermal image was incorrect for an area with the different emissivity. The measured average temperatures of the surface and edge regions were 76.3 ℃ and 102 °C, respectively. Because a micro bolometer was used as the detection element of the infrared camera, the measured temperature represented the far-infrared (7.5–14 μm) emission energy density received by the infrared camera. This result indicates that the emission energy density from the edge region is larger than that from the surface region. The measured average temperature of the gold foils on the sample surface was 28.9 ℃. The

temperature of the gold foils in Fig. 2(b) was much lower than that of the sample surface. Although the gold foils and graphene sample were set to be in contact electrically and thermally, the temperature of the gold foils remained near room temperature (25.3 ℃). This result suggests that the thermal contact between the sample and the gold foil was not low enough for thermal equilibrium, or, the real temperature of graphene should not be very high. Figure 3 shows the power dependences of the measured temperature changes of the surface and edges of the graphene sample and gold foil. The dashed lines indicate the fit obtained using the Stefan–Boltzmann law, which well explained the electrical power dependence of the measured temperature change. This result suggests that direct conversion from electric power to emission power was achieved.

The emission efficiency, α, is introduced in order to consider the electrical power, P [W], which contributed to the far-infrared emission. The emission efficiency α can be estimated using the Stefan–Boltzmann law from the power dependence of the temperature change shown in Fig. 3(a)[25]. Radiant exitance E[28], formerly called radiant emittance[29], which is the energy density of an ideal blackbody, is expressed using α, P [W], emissivity, ε, and radiation area, S [m^2], as follows: .

$$E = \frac{\alpha P}{S} = \varepsilon \sigma T^4, \tag{1}$$

where T is the temperature (K) of blackbody radiation, and σ is the Stefan–Boltzmann constant (J/K). The temperature change ΔT [K] is expressed by the following equation:

$$\Delta T = \sqrt[4]{\frac{\alpha P}{\varepsilon \sigma S} + T_0^4} - T_0, \tag{2}$$

where T_0 is the initial temperature (K). By fitting Eq. (2) to the measured surface temperature change shown in Fig. 3(a), the emission efficiency α was estimated to be 10.2 %. The value of α is very high compared to those of previous biased-graphene emitters[18,23].

Figure 4(a) shows the tilt angle dependence of the temperature change in the surface and edge regions. The temperature change in the edge region is always larger than that in the surface region. Since the measured temperatures described above represented the energy density of far-infrared emission from graphene, the measured temperature of surface and edge regions cannot be compared quantitatively. If the emissivity values for the emission areas can be estimated, it is possible to evaluate the radiation exitance for each area. The

emissivity values are estimated from the FTIR spectra described in the next section. Using the normalized spectrum from 7.5 μm to 14 μm, the emissivity values of the surface and edge regions were estimated to be 0.63 and 0.84, respectively. Figs. 5(a) and (b) show the radiation directivity, the emission angle dependence of the radiant exitance, for the surface and edge regions. The dashed lines in Figs. 5(a) and (b) show the radiation directivity of the conventional material called as "gray body" [30]. Because the dashed line in Fig. 5(a) represents the measured results well, the emission from the surface can be expressed as gray-body-like. In contrast, the radiation directivity of the edge is different from that of a gray body, as shown in Fig. 5(b). Although the radiant exitance from a gray body should be zero in the horizontal direction, which corresponds to a tilt angle of 0° for the edge, the radiant exitance from the edge region was remarkably high at a low tilt angle. The radiant intensity from an ideal blackbody is constant for all emission angles[30]. The results on the edge region in Fig. 4(c) suggest that the radiation directivity from the edge was blackbody-like. The radiation directivities of the surface and edge regions were completely different from each other. The emission mechanisms in both cases should be different.

3.2 FTIR spectrum from biased graphene

Figures 6(a) and (b) show the radiation spectra of the surface and edge regions measured by an FTIR spectrometer (Jasco FT/IR-6600) in air. A broadband blackbody-like spectrum was observed in both cases. The peak wavelengths of both spectra were almost the same, i.e., 10.0 μm. This peak wavelength corresponds to that of the ideal blackbody emission at 289 K, as described by Planck's law. The dashed lines in Figs. 6(a) and (b) show the calculated values of the blackbody spectrum at 289 K. Figure 6(c) shows the spectra of the surface and edge normalized by the ideal blackbody radiation spectrum. As described in the previous section, emissivity values were estimated from these results. The detection limit of the FTIR spectrometer was approximately 30 μm. The low values in the spectra at approximately 7 and 20–30 μm were attributed to the absorption of H_2O in air. The absorption of CO_2 molecules was observed at approximately 15 μm. The dip at approximately 10.5–12.5 μm is due to the influence of the SiC substrate. The influences of SiC on the surface and edges were different. A stronger absorption of SiC was observed in the spectrum of the surface region. The normalized intensity profile of the surface coincides

well with the absorption spectrum of 4H-SiC[31]. This result suggests that the infrared emission from the surface region was a blackbody-like emission strongly scattered by the SiC substrate. However, the emission from the edge was a partially scattered blackbody-like emission. The initial far-infrared waves from the biased graphene sample were emitted in the horizontal direction.

Figures 7(a) and (b) show the power dependence of the total intensity of the spectrum for the surface and edge. In both cases, the total intensity increased linearly with the applied electrical power. These results also suggest that electrical power is directly converted to infrared emission. A notable result was that the peak wavelength of the radiation spectrum was almost constant despite the increase in the applied electrical power, as shown in Figs. 7(c) and (d). The average peak wavelengths of the surface and edge were 10.0 μm. When the real sample temperature increases, the peak wavelength of the blackbody radiation is blue-shifted. The estimated peak wavelengths based on the measured temperature shown in Figs. 3(a) and (b) are plotted as square marks in Figs. 7(c) and (d). The dashed lines represent the calculation results obtained using Wien's displacement law. The estimated peak wavelength of blackbody radiation decreased to approximately 8 μm at 0.4 W. However, the peak wavelengths measured by FTIR were almost constant. This result indicates that the mechanism of emission from graphene is non-thermal. The energy of the peak wavelength measured spectra corresponded to 124 meV. The energy of the surface optical phonon, called the Fuchs–Kliewer (F–K) phonon of SiC, is 117 meV[32,33], and it is close to the measured peak energy. The strong coupling between the graphene plasmon and F–K phonon of SiC was confirmed using HREELS[34,35]. The excitation of graphene plasmons owing to the hot carriers in graphene was theoretically expected[36]. The probable mechanism of far-infrared emission from graphene on SiC by current injection was based on the strong coupling between graphene plasmons generated by hot carriers and the F–K phonons of the SiC substrate. Graphene-plasmon–surface-phonon coupling modes and surface-phonon–plasmon polaritons were generated in graphene on polar substrates and graphene/monolayer sheet heterostructures[37,38]. The momentum transfer caused by scattering in the two-dimensional system may be a cause of the horizontal far-infrared emission of biased graphene on the SiC substrate.

3.3 Emission profile from edge region

The emission intensity distribution of the surface region was uniform. In contrast, the emission profile from the edge region was not uniform. Fig. 8(a) shows a close-up infrared image of the edge region at 0.4 W. Figure 8(b) shows the temperature change profile corresponding to the line shown in Fig. 8(a). The region between the dashed lines in Fig. 8(b) indicates a SiC substrate with a thickness of 515 μm. Because the resolution of the infrared camera was 71 μm/px, it was impossible to resolve the graphene layer. An intensity peak in the temperature change profile was observed at the surface of the sample. This result suggests that infrared waves are emitted from graphene, and that far-infrared waves are emitted horizontally from graphene. A more detailed experiment is required to determine the correct emission profile.

Because the high emission efficiency of graphene on SiC, as described in the previous section, is promising, graphene on SiC has great potential as a far-infrared light emitter with high power. If we can use the other phonon, such as graphene acoustic phonon[39,40], the emission bandwidth will reach to the terahertz range. Furthermore, the nature of non-thermal emission with a constant peak wavelength is suitable for future applications, such as nondestructive inspection.

4. Conclusions

We investigated the infrared emission properties of electrically biased graphene on SiC substrates. The radiation directivity of the graphene surface region was expressed as that for a gray body. The angle dependency of the emission intensity from the surface was the highest at a tilt angle of 0° and monotonically decreased as the tilt angle increased. The radiation directivity of the edge region is different from that of the surface. The maximum emission intensity of the edge is observed at 50°. For all tilt angles, the radiant exitance of the edge was larger than that of the surface. A blackbody-like radiation spectrum with a constant peak wavelength was confirmed for both the surface and edge. The peak wavelengths for both cases were constant at 10.0 μm, regardless of the electrical power. As a result of the electrical power converging to infrared emission, the radiant exitances for both cases linearly increased with the electrical power. The probable explanation for the constant peak wavelength is the coupling of the graphene plasmon induced by the current and F–K phonon of the SiC

substrate. Graphene on SiC realized far-infrared light-emitting diodes using a simple system and provided an excellent platform for the development of high-power far-infrared light emitters.

Acknowledgments

This work was supported by JSPS KAKENHI (grant numbers JP19H02582 and JP21H01394) and the Cooperative Research Project Program of the Research Institute of Communication, Tohoku University.

References

1) K. S. Novoselov, V. I. Fal′ko, L. Colombo, P. R. Gellert, M. G. Schwab and K. Kim, Nature 490, 192 (2012).
2) K. S. Novoselov, A. K. Geim, S. V. Morozov, D. Jiang, Y. Zhang, S. V. Dubonos, I. V. Grigorieve and A. A. Firsov, Science 306, 5696, 666 (2004).
3) K. S. Novoselov, A. K. Geim, S. V. Morozov, D. Jiang, M. I. Katsnelson, I. V. Grigorieva, S. V. Dubonos and A. A. Firsov., Nature 438, 197 (2005).
4) F. Xia, T. Mueller, Y. -M. Lin, A. V. Garcia and P. Avouris, Nat. Nanotechnol. 4, 839 (2009).
5) C. -H. Liu, Y. -C. Chang, T. B. Norris and Z. Zhong, Nat. Nanotechnol. 9, 273 (2014).
6) S. Schuler, J. E. Muench, A. Ruocco, O. Balci, D. V. Thourhout, V. Sorianello, M. Romagnoli, K. Watanabe, T. Taniguchi, I. Goykhman, A. C. Ferrari and T. Mueller, Nat. Commun. 12, 3733 (2021).
7) M. Liu, X. Yin, E. U. -Avila, B. Geng, T. Zentgraf, L. Ju, F. Wang and X. Zhang, Nature 474, 64 (2011).
8) G. Kovacevic, C. Phare, S. Y. Set, M. Lipson and S. Yamashita, Appl. Phys. Express 11, 065102 (2018).
9) D. Ansell, I. P. Radko, Z. Han, F. J. Rodriguez, S. I. Bozhevolnyi and A. N. Grigorenko, Nat. Commun. 6, 8846 (2015).
10) J. Guo, J. Li, C. Liu, Y. Yin, W. Wang, Z. Ni, Z. Fu, H. Yu, Y. Xu, Y. Shi, Y. Ma, S. Gao, L. Tong and D. Dai, Light.: Sci. Apll. 9, 29 (2020).
11) D. Yaday, G. Tamamushi, T. Watanabe, J. Mitsushio, Y. Tobah, K. Sugawara, A. A. Dubinov, A. Satou, M. Ryzhii, V. Ryzhii and T. Otsuji, Nanophotonics 7, 4, 741 (2018).
12) V. Ryzhii, M. Ryzhii, P. P. Maltsev, V. E. Karasik, V. Mitin, M. S. Shur and T. Otsuji, Opt. Express 28, 16, 24136 (2020).

13) L. J. Wong, I. Kaminer, O. Ilic, J. D. Joannopoulos and M. Soljačić, Nat. Photonics 10, 46 (2016).
14) X. Wang, H. Tian, M. A. Mohammad, C. Li, C. Wu, Y. Yang and T. -L. Ren, Nat. Commun. 6, 7767 (2015).
15) M. Freitag, H. -Y. Chiu, M. Steiner, V. Perebeinos and P. Avouris, Nat. Nanotechnol. 5, 497 (2010).
16) S. Berciaud, M. Y. Han, K. F. Mak, L. E. Brus, P. Kim and T. F. Heinz, Phys. Rev. Lett. 104, 227401 (2010).
17) Y. Miyoshi, Y. Fukazawa, Y. Amasaka, R. Reckmann, T. Yokoi, K. Ishida, K. Kawahara, H. Ago and H. Maki, Nat. Commun. 9, 1279 (2018).
18) Y. D. Kim, Y. Gao, R. -J. Shiue, L. Wang, O. B. Aslan, M. -H. Bae, H. Kim, D. Seo, H. -J. Choi, S. H. Kim, A. Nemilentsau, T. Low, C. Tan, D. K. Efetov, T. Taniguchi, K. Watanabe, K. L. Shepard, T. F. Heinz, D. Englund, and J. Hone, Nano Lett. 18, 2, 934 (2018).
19) C. Shi, N. H. Mahlmeister, I. J. Luxmoore and G. R. Nash, Nano Research 11, 3567 (2018).
20) Y. Gong, K. Li, N. Copner, H. Liu, M. Zhao, B. Zhang, A. Pusch, D. L. Huffaker and S. S. Oh, Nanophotonics 10, 4 (2021).
21) Y. Li, P. Ferreyra, A. K. Swan and R. Paiella, ACS Photonics 6, 2562 (2019).
22) L. Kim, S. Kim, P. K. Jha, V. W. Brar and H. A. Atwater, Nat.Mater. 20, 805 (2021).
23) S. -K. Son, M. Šiškins, C. Mullan, J. Yin, V. G Kravets, A. Kozikov, S. Ozdemir, M. Alhazmi, M. Holwill1 and K. Watanabe, 2D Mater. 5 011006 (2017).
24) R. -J. Shiue, Y. Gao, C. Tan, C. Peng, J. Zheng, D. K. Efetov, Y. D. Kim, J. Hone and D. Englund, Nat. Commun. 10, 109 (2019).
25) N. Murakami, Y. Sugiyama, Y. Ohno, and M. Nagase, Jpn. J. Appl. Phys. 60 SCCD01 (2021).
26) T. Aritsuki, T. Nakashima, K. Kobayashi, Y. Ohno and M. Nagase, Jpn. J. Appl. Phys. 55, 06GF03 (2016).
27) L. J. van der PAUW, Philips Res. Respts 13, 1 (1958).
28) F. F. Manza, *Electronics Engineer's Reference Book*, Butterworth-Heinemann, (Oxford, 1989) 6th ed. p. 9/4.
29) S. E. Braslavsky, Pure Appl. Chem. 79, 3, 293-465 (2007).
30) K. J. Havens and E. J. Sharp, *Thermal Imaging Techniques to Survey and Monitor Animals in the Wild*, (Academic Press, Cambridge and Massachusetts, 2016).
31) K. Li, J. M. Fitzgerald, X. Xiao, J. D. Caldwell, C. Zhang, S. A. Maier, X. Li and V. Giannini, ACS Omega 2, 7, 3640 (2017).
32) H. Nienhaus, T. U. Kampen, W. Mönch, Surface Science 324, 1, L328 (1995).
33) J. Lu, K. P. Loh, H. Huang, W. Chen and A. T. S. Wee, Phys. Rev.80,113410 (2009).
34) I. Kaminer, Y. T. Katan, H. Buljan, Y. Shen, O. Ilic, J. J. López, L. J. Wong, J. D. Joannopoulos and M. Soljačić, Nat. Commun. 7, 11880 (2016).
35) R. J. Koch, Th. Seyller and J. A. Schaefer, Phys. Rev. B 82, 201413(R) (2010).
36) R. J. Koch, S. Fryska, M. Ostler, M. Endlich, F. Speck, T. Hänsel, J. A. Schaefer, and Th.

Seyller, Phys. Rev. Lett. 116, 106802 (2016).
37) V. W. Brar, M. S. Jang, M. Sherrott, S. Kim, J. J. Lopez, L. B. Kim, M. Choi and H. Atwater, Nano Lett. 14, 7, 3876 (2014).
38) Y. Jia, H. Zhao, Q. Guo, X. Wang, H. Wang and F. Xia, ACS Photonics 2, 7, 907 (2015).
39) E. H. Hwang and S. D. Sarma, Phys. Rev. B77, 115449 (2008).
40) K. Kaasbjerg, K. S. Thygesen and K. W. Jacobsen, Phys. Rev. B85,165440 (2012).

Figure Captions

Fig. 1. (a) Schematic of the device structure. The size of the graphene sample was 10 × 10 mm^2. Two electrodes were used for injecting current into graphene, and the other electrodes were used for measuring the voltage applied to graphene in van der Paul configuration. Gold foils were placed between the graphene sample and electrodes to obtain a good contact. (b) Schematic of the experimental method in this study. ~~The light~~ Far-infrared emission from graphene on SiC was observed by an infrared camera. Graphene on SiC was fixed on a tilting stage by electrodes. The tilt angle of graphene, θ, was defined as the angle between the normal to the graphene surface and infrared camera.

Fig. 2. (a) Optical image of graphene on SiC at a tilt angle of 60°. The regions surrounded by the blue and red squares indicate the graphene surface and edge, respectively. (b) Infrared image of graphene on SiC at 0.4 W and θ = 60°. Since a micro bolometer was used as the detection element of the infrared camera, measured temperature means the infrared energy density received by the infrared camera. Infrared energy density emitted from the graphene edge was larger than that from the surface.

Fig. 3. Electrical power dependences of temperature changes for surface and edge region. In both cases, the temperature linearly increased with applied electrical power. Dashed lines show the theoretical values estimated by fitting the Stefan–Boltzmann law (Eq. 2) to the measured temperature change. Since the surface area was 100 mm^2, the emission efficiency of the graphene surface, α, could be calculated from the fit, i.e., α = 10.2%. The

green dots indicate the data of the gold foil in contact with the graphene surface. The insignificant increase in gold foil temperature indicated that the real temperature of graphene should be low.

Fig. 4. (a) Angle dependence of temperature change at the graphene surface (blue dot) and graphene edge (red dot). The infrared energy density from the edge was larger than that from the surface.

Fig. 5. Radiation directivities of (a) surface and (b) edge regions obtained using emissivity values of surface and edge regions, i.e., 0.63 and 0.84, estimated from Figs. 6(a) and (b), respectively. The dashed lines indicate the radiation directivity of a gray body. Radiation directivity of the surface region corresponded to that of a gray body. However, radiation directivity of the edge region was different from that of a gray body. Since radiant exitance of the edge region at low angles only slightly decreased, radiation directivity of the edge region was blackbody-like.

Fig. 6. Emission spectra from (a) surface and (b) edge region at 200 V (0.4 W) measured by FTIR. Both spectra were blackbody-like. The dashed lines show the ideal blackbody radiation spectrum calculated from Planck's law at 289 K, which corresponds to a peak wavelength of 10.0 μm because the peak wavelengths of the measured spectra were 10.0 μm. The detection limit of the FTIR spectrometer was approximately 30 μm. The low values of the spectra at approximately 7 and 20–30 μm are attributed to H_2O absorption. The dip at approximately 15 μm is attributed to CO_2 absorption. The dip around 10.5–12.5 μm is due to the influence of the SiC substrate. (c) Spectra of the surface (blue line) and edge (red line) regions normalized with the ideal blackbody spectrum. The estimated emissivity values in the range of 7.5–14 μm wavelength for the surface and edge were 0.63 and 0.84, respectively.

Fig. 7. Electrical power dependence of total intensity for (a) surface and (b) edge regions. In both cases, the total intensities linearly increased with applied electrical power. Electrical power dependence of the peak wavelength of emission spectra for (c) surface

and (d) edge. The solid line shows the average of the measured peak wavelength. The average peak wavelengths of the surface and edge were 10.0 μm. The green squares in Figs. 6(c) and (d) show the estimated peak wavelengths based on the measured temperature shown in Figs. 3(a) and (b). The dashed lines show the theoretical values of blackbody radiation obtained by fitting Wien's displacement law to the measured temperature change. The results in Figs. 6(c) and (d) show that the mechanism of emission from graphene was non-thermal.

Fig. 8. (a) Infrared image of graphene edge at 0.4 W. (b) Line profile of temperature change from A to A' shown in Fig. 7 (a). The left dashed line corresponds to the graphene surface, and the right dashed line corresponds to the bottom of the SiC substrate. The thickness of the SiC substrate was 515 μm. The resolution of the infrared camera was 71 μm/px.

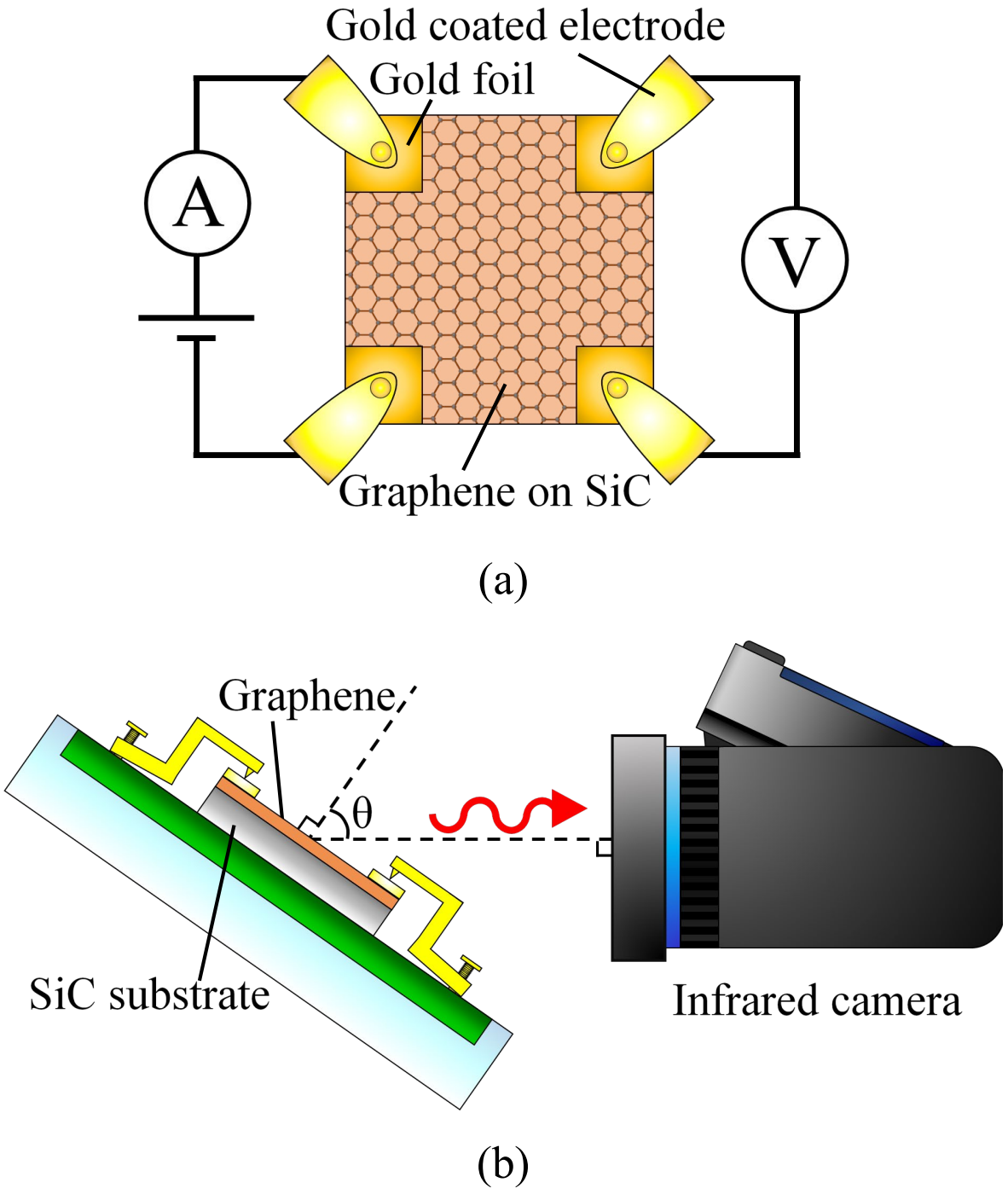
Gold coated electrode
Gold foil
A
V
Graphene on SiC
(a)
Graphene
θ
SiC substrate
Infrared camera
(b)

Fig. 1.

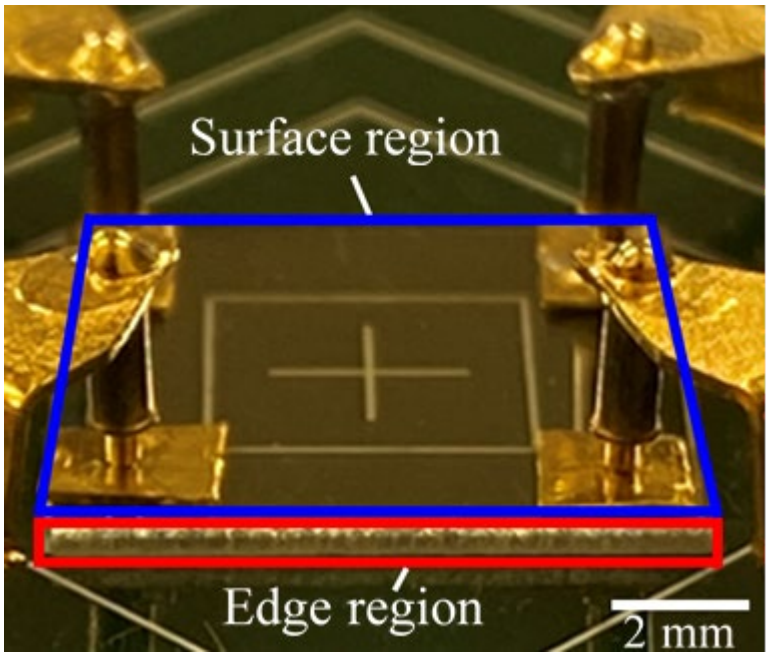

(a)

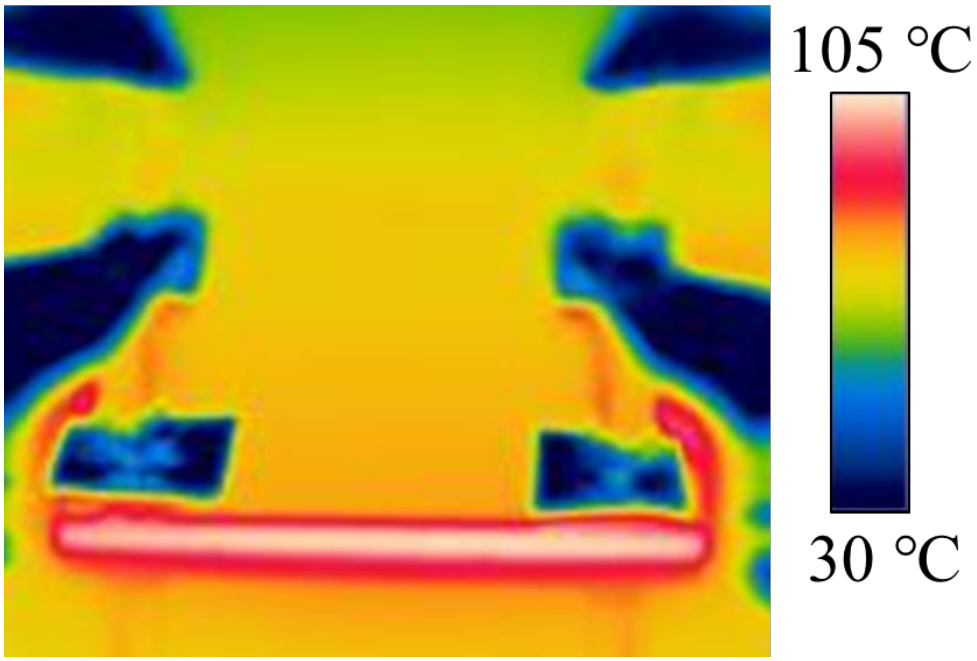

(b)

Fig. 2.

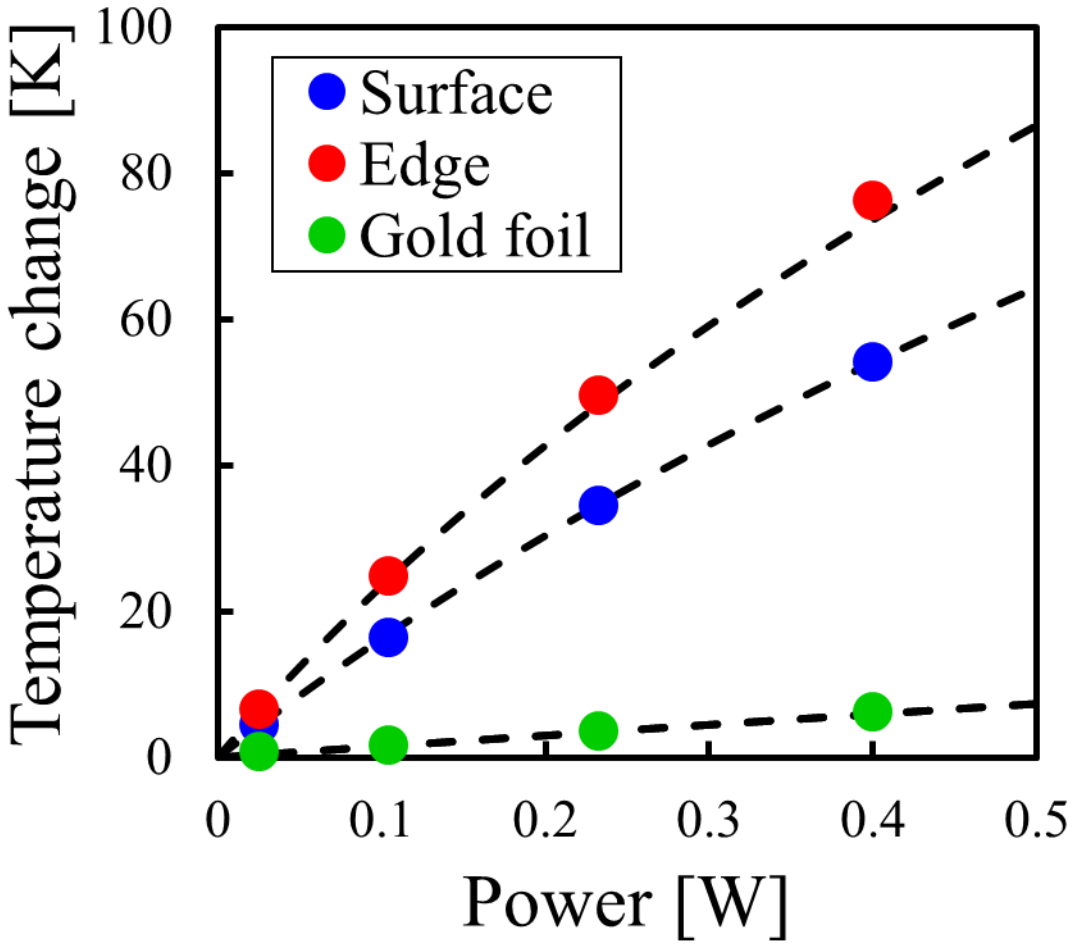
Temperature change [K]
100
80
60
40
20
0
Surface
Edge
Gold foil
0
0.1
0.2
0.3
0.4
0.5
Power [W]

Fig. 3.

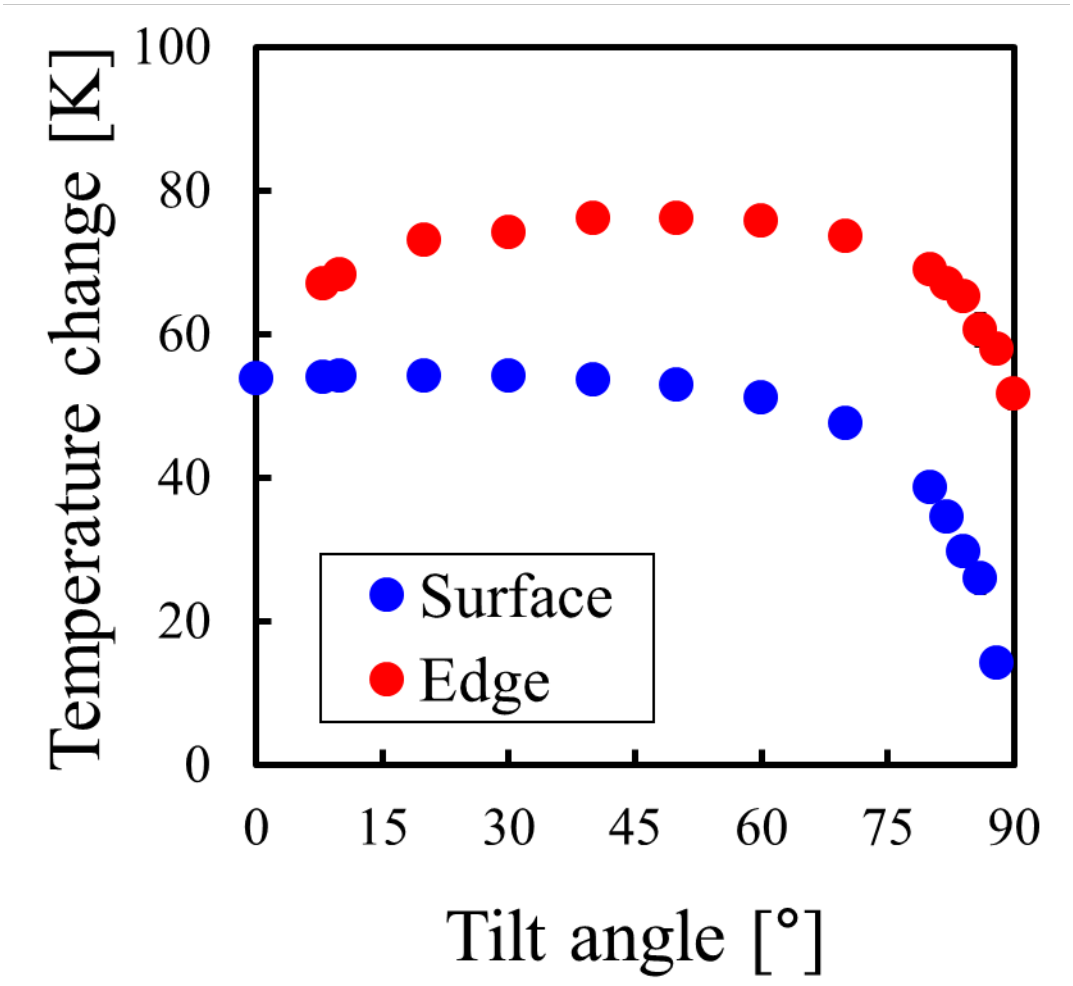
Temperature change [K]
100
80
60
40
20
0
0
15
30
45
60
75
90
Tilt angle [°]
Surface
Edge

Fig. 4.

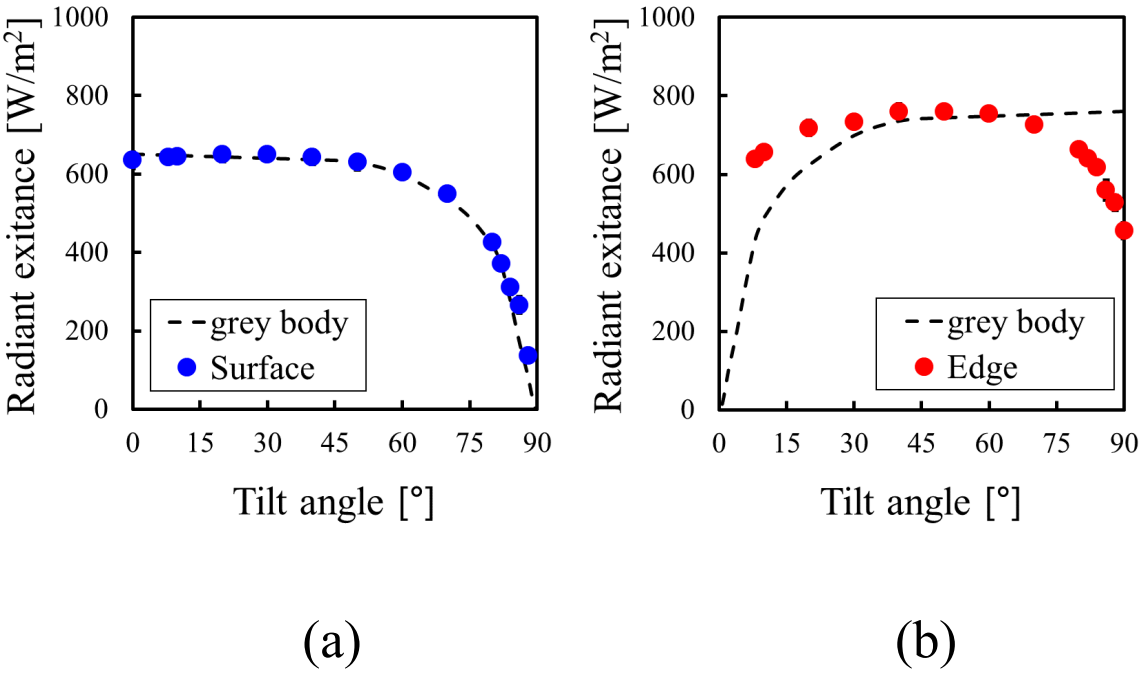
Radiant exitance [W/m2]
1000
800
600
400
200
0
0
15
30
45
60
75
90
Tilt angle [°]
grey body
Surface
Radiant exitance [W/m2]
1000
800
600
400
200
0
0
15
30
45
60
75
90
Tilt angle [°]
grey body
Edge

(a) (b)

Fig. 5.

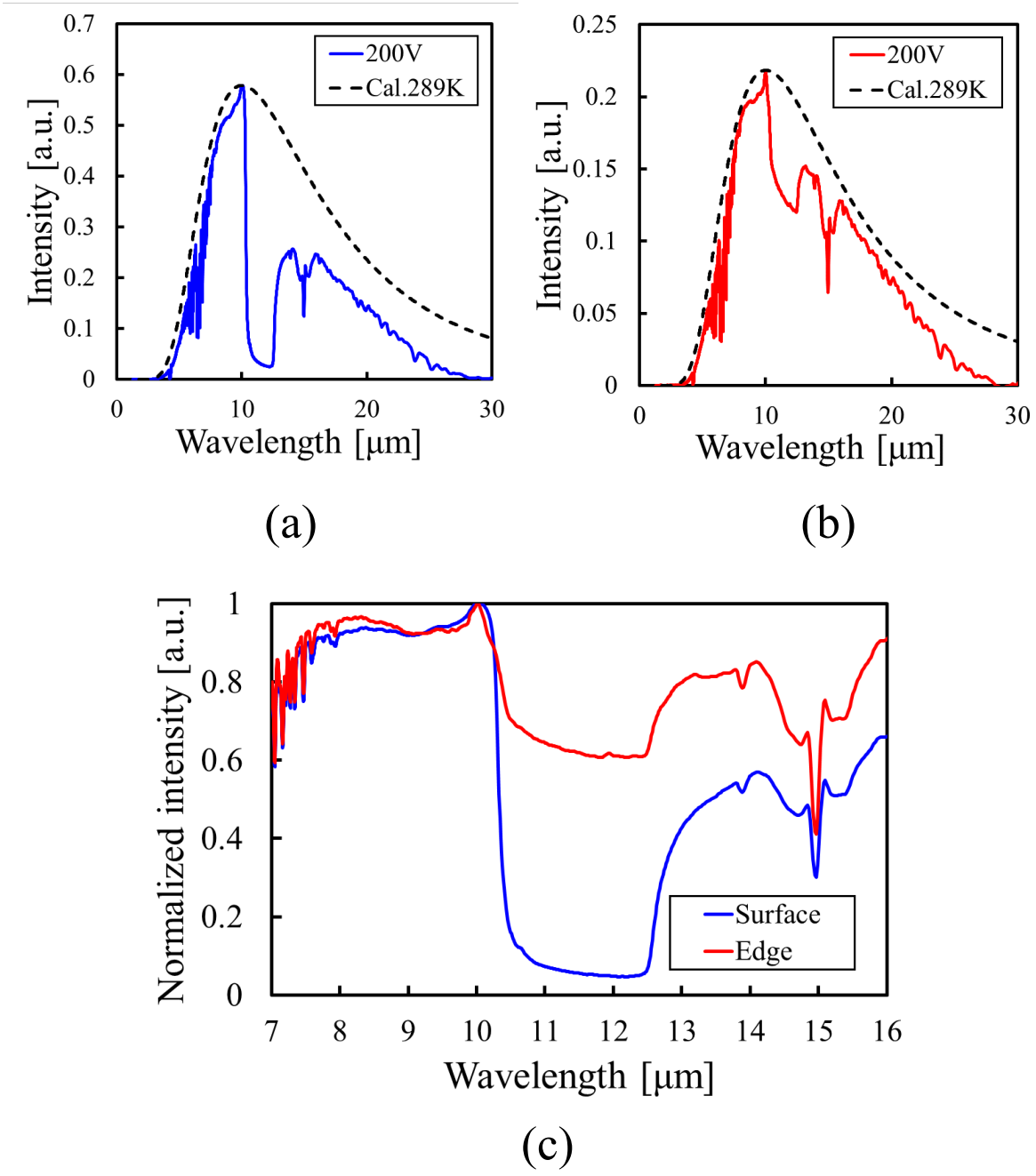
0.7
0.6
0.5
0.4
0.3
0.2
0.1
0
Intensity [a.u.]
200V
Cal.289K
0
10
20
30
Wavelength [μm]
(a)
0.25
0.2
0.15
0.1
0.05
0
Intensity [a.u.]
200V
Cal.289K
0
10
20
30
Wavelength [μm]
(b)
1
0.8
0.6
0.4
0.2
0
Normalized intensity [a.u.]
Surface
Edge
7
8
9
10
11
12
13
14
15
16
Wavelength [μm]
(c)

Fig. 6.

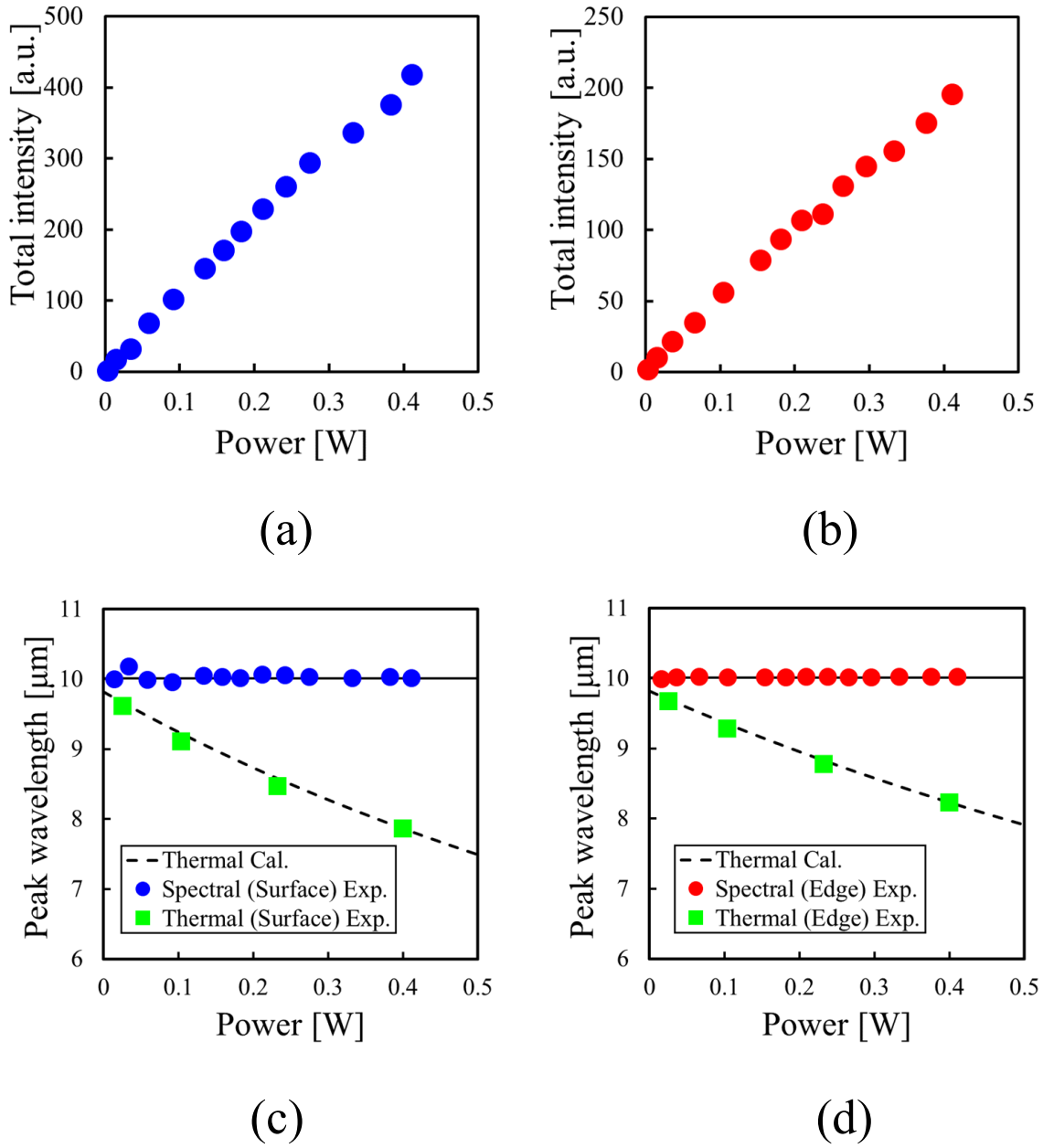
Total intensity [a.u.]
Power [W]
(a)
(b)
Peak wavelength [μm]
Thermal Cal.
Spectral (Surface) Exp.
Thermal (Surface) Exp.
Spectral (Edge) Exp.
Thermal (Edge) Exp.
(c)
(d)

Fig. 7.

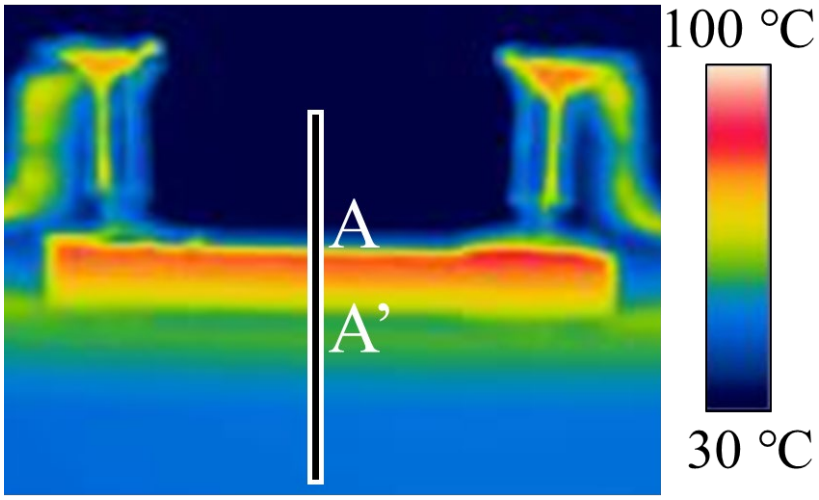
100 °C
A
A'
30 °C

(a)

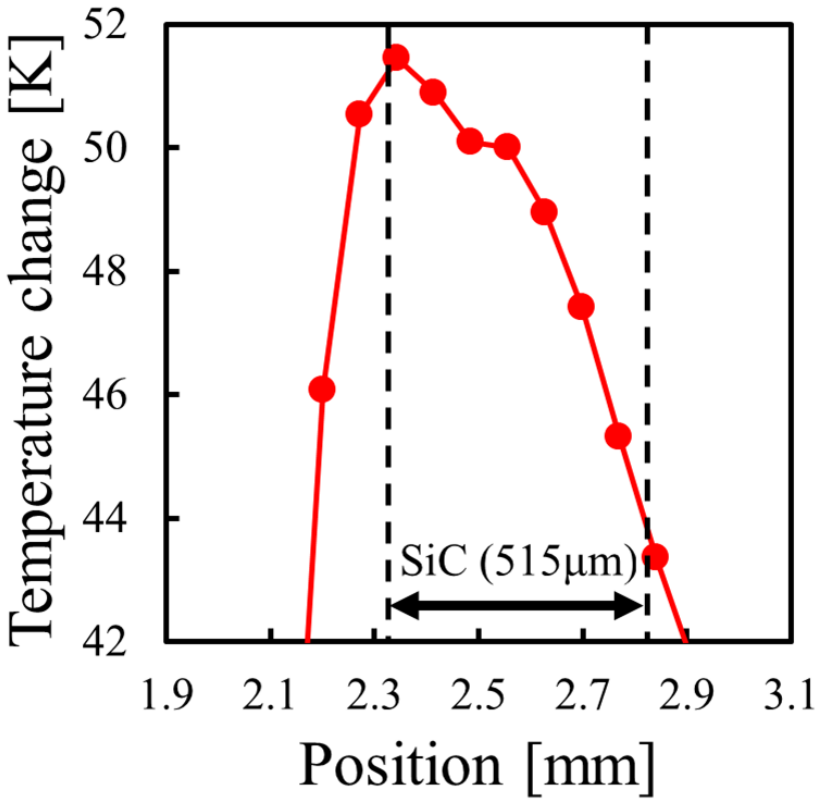
Temperature change [K]
52
50
48
46
44
42
SiC (515μm)
1.9
2.1
2.3
2.5
2.7
2.9
3.1
Position [mm]

(b)

Fig. 8.